

# A Robust Deadbeat Predictive Current Control Method for IPMSM

Xiaoyan Huang, *Member, IEEE*, Qichao Hu, Zixuan Liu, Weny Li, Geng Yang, *Member, IEEE*, Zhaokai Li, *Member, IEEE*

**Abstract**—Deadbeat predictive current control (DPCC) demonstrates excellent dynamic performance. However, in practical applications, its effectiveness is degraded by parameter mismatches and inverter nonlinearities. Among the various improvement methods addressed for these issues, incremental model-based DPCC (I-DPCC) achieves zero static current error with a low computational burden but suffers from instability under parameter variation, especially when applied to interior permanent magnet synchronous motors (IPMSMs). In this paper, a robust I-DPCC (RI-DPCC) combining feedforward control is proposed for IPMSM, with an adjustable stable operation range that can be extended to twice the actual inductance or even larger. To further improve the robustness of dynamic performance, an inductance correction method is introduced to track the variation of inductance during dynamic processes. Thus, the current commands can be well tracked even when significant inductance variation occurs. With sufficient voltage margin, the dynamic processes under mismatched inductance can be shortened to four control periods. Finally, experimental results validate the effectiveness of the proposed method.

**Index Terms**—Deadbeat predictive current control (DPCC), parameter mismatch, incremental model-based, permanent magnet synchronous motor (PMSM).

## I. INTRODUCTION

MONG various current control methods for permanent magnet synchronous motors (PMSMs), deadbeat predictive current control (DPCC) demonstrates excellent dynamic performance with low computational burden and current ripples. However, inevitable parameter mismatches cause voltage commands to deviate from their expected values. Meanwhile, factors such as delays and inverter nonlinearities in the practical system lead to errors between voltage commands and the actual voltages applied to the motor. Under conventional DPCC (C-DPCC), these two types of errors not only cause static current errors but also degrade the dynamic performance. The current loop will even be unstable when the estimated inductance adopted by regulators exceeds twice its actual value

This work was supported in part by the National Key R&D Program of China (2019YFE0123500), in part by the National Natural Science Foundation of China (51837010) and in part by the Zhejiang Provincial Natural Science Foundation of China (No. LQ22E070003).

Xiaoyan Huang, Qichao Hu, Zixuan Liu and Weny Li are with the Zhejiang Provincial Key Laboratory of Electrical Machine Systems, College of Electrical Engineering, Zhejiang University, Hangzhou 310027, China (e-mail: xiaoyanhuang@zju.edu.cn; eehqc@zju.edu.cn; eelzx@zju.edu.cn; yazu0226@zju.edu.cn).

Geng Yang is with the State Key Laboratory of Fluid Power and Mechatronic Systems, School of Mechanical Engineering, Zhejiang University, Hangzhou 310027, China (e-mail: yanggeng@zju.edu.cn).

Zhaokai Li is with the Department of Electrical Engineering, KTH Royal Institute of Technology, Stockholm, 11428, Sweden (zhaokai@kth.se).

[1]. Therefore, researchers have proposed extensive methods to improve the performance and robustness of C-DPCC, which can be mainly divided into three categories.

The first category is to shorten delays. For C-DPCC, the theoretical tracking delay of two control periods consists of a unit delay resulting from computation and PWM updating, and another from the action of voltages [2]. By updating the duty ratio of PWM at the middle instant of each control period, the theoretical tracking delay can be shortened to one and a half control periods [3]. Furthermore, the unit computation delay can be avoided by using field-programmable gate arrays with parallel computing capability [4] [5]. The oversampling technique on current and speed applied in [5] also effectively improves the stability robustness. Another common delay is the phase delay attached to the coordinate transformation from  $dq$ -axes to  $\alpha\beta$ -axes during the modulation process, which influences the action of voltages, especially at low switching frequencies. Therefore, the authors in [6] deduce the control equations directly from an exact discretization model of the surface PMSM (SPMSM) in the  $\alpha\beta$ -reference frame. Thus, the phase delay mentioned above can be fundamentally eliminated. However, these methods require high hardware performance and lack improvements in performance robustness.

The second category is voltage compensation. These methods use available command and feedback values of currents and voltages to compensate for the voltage commands and eliminate static current errors. This compensation can be made through simple calculations, based on the mathematical model of PMSM, or as a result of complex disturbance observers. In [7], a parallel integrator is introduced to compensate for the voltage commands calculated by C-DPCC, but the slowdown of dynamic response is inevitable. In [8], the authors use fuzzy algorithms to adjust the weight of C-DPCC and proportional integral (PI) control under different working conditions so that their merits can be combined, although the parameters of fuzzy algorithms are quite complex to tune.

A typical improvement method based on the mathematical model of PMSM is incremental model-based DPCC (I-DPCC). The essential improvement of I-DPCC, adopted in [3] and [9]–[11], is the introduction of a built-in integrator, which enables excellent dynamic performance under matched parameters and zero static current error under parameter mismatches. However, its narrow stable operation range limits practical applications. Another improvement method, proposed in [12], adds feedforward terms to compensate for static current errors and a noise suppression scheme to enhance stability robustness, but the dynamic performance under mismatched

parameters still deteriorates.

For methods that construct disturbance observers, both voltage errors caused by parameter mismatches and inverter nonlinearities can be modeled and observed as disturbances. Various kinds of disturbance observers can be designed to compensate for voltages and make predictions on currents, such as Luenberger observer [4] [5], sliding mode observer [13]- [15], extended state observer [16] [17], and so on. Although disturbance observers make it possible for the current loop to maintain excellent dynamic performance without static error under disturbances, the difficulty of tuning parameters, the complexity of observers, and the computational burden limit their practical applications.

The third category is parameter estimation. With relatively accurate estimated parameters, problems resulting from parameter mismatches can be fundamentally solved. Parameter estimation can be performed offline or online. As an offline method, the look-up table method based on the finite element simulation results applied in [18] can take the saturation effects of inductance into account, but it has high storage costs, poor portability, and takes a long time to establish. Therefore, more precise and considerate parameter estimation should be done online.

If multiple parameters are estimated online simultaneously, such as in [19], where full parameters of the motor are estimated in the  $\alpha\beta$ -reference frame, the implementation of algorithms can be rather complex. Since I-DPCC is free of rotor flux linkage and has been proven to have zero static current error under mismatched resistance and inductance, the parameters that need to be estimated can be reduced to only inductance for dynamic performance improvement [9]. Online parameter estimation methods include recursive least squares-based algorithm [9] [19], disturbance observer-based inductance extraction algorithm [10] [11], extended Kalman filter-based algorithm [20], and so on. However, degradation of dynamic performance under parameter variation is still inevitable due to the tracking delay of estimated results.

Although existing methods have made substantial improvements, there is little published literature focused on DPCC for IPMSMs with significant inductance variation, as the issues of dynamic performance degradation and instability remain intractable. Therefore, this paper proposes a robust I-DPCC (RI-DPCC) method with inductance correction focused on improving the dynamic performance of the current loop for IPMSMs, considering both stability and performance robustness.

In this paper, the closed-loop transfer function of C-DPCC is first derived, and its parameter robustness is theoretically analyzed. Then, the principle of RI-DPCC with four adjustable feedforward coefficients is introduced. By combining feedforward control, its stable operation range can be extended to twice the actual inductance or even larger, while maintaining zero static current error even under mismatched parameters. After that, an inductance correction method based on the responses of currents is added to track the variation of inductance during dynamic processes. Thus, the current commands can be well tracked under the proposed method, even when significant inductance variation occurs. With sufficient voltage

margin, the dynamic processes under mismatched inductance can be shortened to four control periods, while maintaining a tracking delay of two control periods under accurate motor parameters. Finally, the effectiveness of the proposed method is validated through experiments on the test IPMSM.

## II. CONVENTIONAL DEADBEAT PREDICTIVE CURRENT CONTROL AND PARAMETER ROBUSTNESS ANALYSIS

### A. Principles of C-DPCC

The mathematical model of IPMSM in the  $dq$ -reference frame can be expressed as follows [10]:

$$\mathbf{u}_{dq} = \begin{bmatrix} R + L_d p & -\omega_e L_q \\ \omega_e L_d & R + L_q p \end{bmatrix} \mathbf{i}_{dq} + \begin{bmatrix} 0 \\ \omega_e \psi_f \end{bmatrix} \quad (1)$$

where  $\mathbf{u}_{dq} = [u_d \ u_q]^T$  and  $\mathbf{i}_{dq} = [i_d \ i_q]^T$  denote the  $dq$ -axis voltages and currents, respectively; and  $p$ ,  $\omega_e$ ,  $R$ ,  $\psi_f$ ,  $L_d$  and  $L_q$  denote the derivative operator, electrical angular velocity, stator resistance, rotor flux linkage,  $d$ -axis and  $q$ -axis inductances, respectively. For SPMMSMs,  $L_d$  approximately equals  $L_q$ , namely  $L_d = L_q = L$ .

In order to implement predictive current control algorithms in digital systems, the discrete expression of  $\mathbf{i}_{dq}$  can be obtained as follows using the forward Euler method.

$$\mathbf{i}_{dq}(k+1) = \mathbf{G}(k) \mathbf{i}_{dq}(k) + \mathbf{H} [\mathbf{u}_{dq}(k) - \Psi(k)] \quad (2)$$

where  $\mathbf{i}_{dq}(k) = [i_d(k) \ i_q(k)]^T$ ,  $\mathbf{u}_{dq}(k) = [u_d(k) \ u_q(k)]^T$ ,

$$\mathbf{G}(k) = \begin{bmatrix} 1 - \frac{T_s R}{L_d} & \frac{L_q}{L_d} T_s \omega_e(k) \\ -\frac{L_d}{L_q} T_s \omega_e(k) & 1 - \frac{T_s R}{L_q} \end{bmatrix}, \quad \mathbf{H} = \begin{bmatrix} \frac{T_s}{L_d} & 0 \\ 0 & \frac{T_s}{L_q} \end{bmatrix},$$

and  $\Psi(k) = [0 \ \omega_e(k) \psi_f]^T$ ;  $i_{dq}(k)$  and  $\omega_e(k)$  denote the  $dq$ -axis currents and electrical angular velocity at the  $k^{th}$  instant, respectively;  $\mathbf{u}_{dq}(k)$  denotes the  $dq$ -axis voltages applied during the  $k^{th}$  control period;  $T_s$  denotes the control period.

For microprocessor-based digital systems, it is necessary to compensate for the control delay caused by computation and PWM updating. Since the mechanical time constant is usually much larger than the electrical time constant and  $T_s$  is short enough, one can assume that  $\omega_e$  stays constant during two adjacent control periods, i.e.,  $\omega_e(k+1) = \omega_e(k)$ . Then, during the  $k^{th}$  control period, C-DPCC predicts  $\hat{\mathbf{i}}_{dq}(k+1)$  using (3) and calculates voltage commands  $\mathbf{u}_{dq}^*(k+1)$  for the next control period using (4), aiming at tracking current commands  $\mathbf{i}_{dq}^*(k)$  with a delay of  $2T_s$ . Thus, (3) and (4) comprise the control equations of C-DPCC.

$$\hat{\mathbf{i}}_{dq}(k+1) = \hat{\mathbf{G}}(k) \hat{\mathbf{i}}_{dq}(k) + \hat{\mathbf{H}} [\mathbf{u}_{dq}^*(k) - \hat{\Psi}(k)] \quad (3)$$

$$\mathbf{u}_{dq}^*(k+1) = \hat{\mathbf{H}}^{-1} [\hat{\mathbf{i}}_{dq}^*(k) - \hat{\mathbf{G}}(k) \hat{\mathbf{i}}_{dq}(k+1)] + \hat{\Psi}(k) \quad (4)$$

where  $\mathbf{u}_{dq}^*$  and  $\mathbf{i}_{dq}^*$  denote the command values of  $dq$ -axis voltages and currents, respectively;  $\hat{\mathbf{i}}_{dq}$  and  $\hat{\mathbf{X}}$  denote the estimated values of  $dq$ -axis currents and motor parameters ( $X = R, L_{d,q}, \psi_f$ ), respectively; subsequently,  $\hat{\mathbf{G}}(k)$ ,  $\hat{\mathbf{H}}$  and  $\hat{\Psi}(k)$  are defined as the expressions of  $\mathbf{G}(k)$ ,  $\mathbf{H}$  and  $\Psi(k)$  when substituting estimated motor parameters, i.e.,

$$\hat{\mathbf{G}}(k) = \begin{bmatrix} 1 - \frac{T_s \hat{R}}{\hat{L}_d} & \frac{\hat{L}_q}{\hat{L}_d} T_s \omega_e(k) \\ -\frac{\hat{L}_d}{\hat{L}_q} T_s \omega_e(k) & 1 - \frac{T_s \hat{R}}{\hat{L}_q} \end{bmatrix}, \quad \hat{\mathbf{H}} = \begin{bmatrix} \frac{T_s}{\hat{L}_d} & 0 \\ 0 & \frac{T_s}{\hat{L}_q} \end{bmatrix},$$

and  $\hat{\Psi}(k) = [0 \quad \omega_e(k) \hat{\psi}_f]^T$ .

### B. C-DPCC Parameter Robustness Analysis

Since the performance of current loop is usually tested at a constant speed, it is reasonable to consider matrices  $\mathbf{G}$  and  $\Psi$  as constants for analysis. By transforming equations (2), (3), and (4) into the  $z$ -domain and eliminating the intermediate voltage quantities, the closed-loop discrete transfer function of the current loop under C-DPCC can be obtained as (5) based on the control block diagram shown in Fig. 1, where the voltage limitation is not considered. Here,  $e_{dq}(z)$  is defined as  $(\mathbf{u}_{dq}^*(z) - \hat{\Psi}(z)) - (\mathbf{u}_{dq}(z) - \Psi(z))$  to take inverter nonlinearities into account.

$$\mathbf{i}_{dq}(z) = \mathbf{M}_1^{-1}(z) [\mathbf{H} \hat{\mathbf{H}}^{-1} \mathbf{i}_{dq}^*(z) - \mathbf{H} (\mathbf{I} z + \hat{\mathbf{G}}) \mathbf{e}_{dq}(z)] \quad (5)$$

where

$$\mathbf{M}_1(z) = \mathbf{I} z^2 + (\hat{\mathbf{G}} - \mathbf{G}) z + \hat{\mathbf{G}} (\mathbf{H} \hat{\mathbf{H}}^{-1} \hat{\mathbf{G}} - \mathbf{G})$$

and  $\mathbf{I}$  denotes the second-order identity matrix.

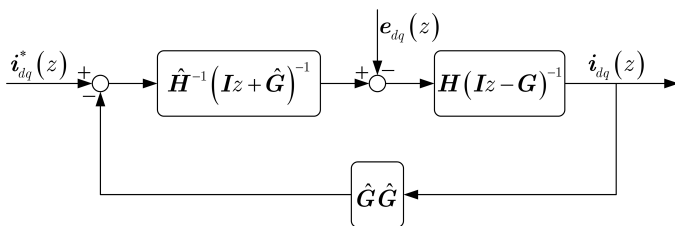


Fig. 1. Control block diagram of the current loop under C-DPCC.

With accurate motor parameters and voltage errors caused by inverter nonlinearities being temporarily ignored, (5) can be simplified to  $\mathbf{i}_{dq}(z) = z^{-2} \mathbf{i}_{dq}^*(z)$ . It has two poles placed at the origin of the  $z$ -domain and a static gain of 1, indicating a tracking delay of  $2T_s$  for dynamic response and zero static current error. However, inevitable parameter mismatches not only cause static current errors but also degrade the dynamic performance. The stability of the current loop under C-DPCC is determined by the pole distribution of  $\mathbf{M}_1^{-1}(z)$ , indicating that  $\omega_e$ ,  $T_s$ , estimated and actual values of  $R$ ,  $L_d$ , and  $L_q$  are all the influencing factors. By ignoring  $R$ , whose impact is relatively slight on stability as  $RT_s/L_{d(q)} \ll 1$ , and  $(T_s \omega_e)^2$ , which is close to zero at low speeds due to high control frequency, (5) can be approximated to (6) since the stability of C-DPCC is mostly sensitive to the error in inductance.

$$\begin{bmatrix} \mathbf{i}_d(z) \\ \mathbf{i}_q(z) \end{bmatrix} \approx \begin{bmatrix} A_{1d}(z)B_{1d}(z) \\ A_{1q}(z)B_{1q}(z) \end{bmatrix} + A_{1d}(z)A_{1q}(z)T_s \omega_e \underbrace{\begin{bmatrix} -C_{1q}(z)B_{1q}(z) \\ C_{1d}(z)B_{1d}(z) \end{bmatrix}}_{\text{coupling part}} \quad (6)$$

where

$$\begin{aligned} A_{1d(1q)}(z) &= (z^2 + \delta L_{d(q)})^{-1} \\ B_{1d(1q)}(z) &= \frac{\hat{L}_{d(q)}}{L_{d(q)}} i_{d(q)}^*(z) - \frac{T_s}{L_{d(q)}} (z+1) e_{d(q)}(z) \\ C_{1d(1q)}(z) &= \frac{\hat{L}_{d(q)}}{\hat{L}_{q(d)}} (z + \delta L_{d(q)}) - \frac{L_{d(q)}}{L_{q(d)}} (z - \delta L_{d(q)}) \end{aligned}$$

and  $\delta L_{d(q)}$  denotes the relative error of  $dq$ -axis inductances, which is defined as  $(\hat{L}_{d(q)} - L_{d(q)})/L_{d(q)}$ .

Then, according to (6) and the Jury stability criterion, the estimated inductance adopted by regulators of C-DPCC should satisfy (7) to ensure stable operation [21]. This range can meet the stability needs in most applications, but the current loop may still be unstable when the actual inductance decreases to below half the unchanged estimated value. Meanwhile, with an increase in inductance errors, the poles of  $\mathbf{M}_1^{-1}(z)$  will gradually deviate from the origin, resulting in reduced dynamic performance such as slowdowns, overshoots, and oscillations. All these drawbacks of C-DPCC listed above should be considered when making improvements.

$$0 < \hat{L}_{d(q)}/L_{d(q)} < 2 \quad (7)$$

### III. ROBUST INCREMENTAL MODEL-BASED DEADBEAT PREDICTIVE CURRENT CONTROL AND PROPOSED METHOD

#### A. Principles of I-DPCC and RI-DPCC

The incremental model-based expression of  $\mathbf{i}_{dq}$  can be obtained as follows by subtracting (2) at two adjacent instants. Since  $\omega_e(k-1)$  is considered equal to  $\omega_e(k)$ , the use of  $\psi_f$  can be eliminated [11].

$$\Delta \mathbf{i}_{dq}(k+1) = \mathbf{G}(k) \Delta \mathbf{i}_{dq}(k) + \mathbf{H} \Delta \mathbf{u}_{dq}(k) \quad (8)$$

where  $\Delta \mathbf{i}_{dq}(k) = \mathbf{i}_{dq}(k) - \mathbf{i}_{dq}(k-1)$  and  $\Delta \mathbf{u}_{dq}(k) = \mathbf{u}_{dq}(k) - \mathbf{u}_{dq}(k-1)$ .

Similar to the derivation process of C-DPCC, I-DPCC also consists of equations for current prediction and voltage command calculation. As a feedback control method, I-DPCC can achieve zero static current error even under mismatched motor parameters, but it suffers from poor stability robustness. If the feedback of  $\mathbf{i}_{dq}^*(z)$  can be fully replaced by the feedforward of  $\mathbf{i}_{dq}^*(z)$ , the current loop will become an open-loop system that remains stable regardless of the severity of parameter mismatches [22]. However, single feedforward control cannot address the static current errors caused by model misalignment.

To combine their merits and avoid the demerits,  $\mathbf{i}_{dq}(k)$  and  $\hat{\mathbf{i}}_{dq}(k+1)$ , which play the role of feedback values in the control equations of DPCC, are partially replaced by the feedforward values  $\hat{\mathbf{i}}_{dq}(k)$  and  $\hat{\mathbf{i}}_{dq}^*(k-1)$  separately. Two coefficient matrices,  $\mathbf{F}_1$  and  $\mathbf{F}_2$ , are introduced to adjust the weight of feedforward values during the control process. The feedforward values are only added to the uncoupled part of currents, as adding them to the coupling part did not show an obvious positive impact on further extending the stable range in simulations. The control equations of RI-DPCC are then given by (9) and (10) as follows. When  $\mathbf{F}_1 = \mathbf{F}_2 = \mathbf{0}$ , they

comprise the control equations of I-DPCC without feedforward values.

$$\begin{aligned} \Delta\hat{\mathbf{i}}_{dq}(k+1) \\ = \hat{\mathbf{G}}(k)\Delta\mathbf{i}_{dq}(k) + \hat{\mathbf{H}}\Delta\mathbf{u}_{dq}^*(k) + \mathbf{F}_1(\hat{\mathbf{i}}_{dq}(k) - \mathbf{i}_{dq}(k)) \quad (9) \end{aligned}$$

$$\begin{aligned} \hat{\mathbf{i}}_{dq}(k+1) &= \mathbf{i}_{dq}(k) + \Delta\hat{\mathbf{i}}_{dq}(k+1) \\ \Delta\mathbf{u}_{dq}^*(k+1) \\ = \hat{\mathbf{H}}^{-1} &\left\{ \begin{array}{l} \mathbf{i}_{dq}^*(k) - \hat{\mathbf{i}}_{dq}(k+1) - \hat{\mathbf{G}}(k)\Delta\hat{\mathbf{i}}_{dq}(k+1) \\ - \mathbf{F}_2(\mathbf{i}_{dq}^*(k-1) - \hat{\mathbf{i}}_{dq}(k+1)) \end{array} \right\} \quad (10) \\ \mathbf{u}_{dq}^*(k+1) &= \mathbf{u}_{dq}^*(k) + \Delta\mathbf{u}_{dq}^*(k+1) \end{aligned}$$

where  $\mathbf{F}_{1(2)} = \begin{bmatrix} f_{d1(d2)} & 0 \\ 0 & f_{q1(q2)} \end{bmatrix}$ ;  $f_{d1,d2,q1,q2}$  are the concrete feedforward coefficients.

### B. RI-DPCC Parameter Robustness Analysis

The control block diagram of the current loop under RI-DPCC is shown in Fig. 2, based on the  $z$ -domain expressions of (2), (9), and (10). Here, voltage errors caused by inverter nonlinearities are still considered, and  $e_{dq}(z)$  is defined as  $\mathbf{u}_{dq}^*(z) - (\mathbf{u}_{dq}(z) - \Psi(z))$ , since  $\hat{\Psi}(z)$  is no longer required by the control equations. Then, the corresponding closed-loop discrete transfer function can be obtained as:

$$\mathbf{i}_{dq}(z) = \mathbf{M}_2^{-1}(z) \left[ \frac{(\mathbf{I}z - \mathbf{F}_1)(\mathbf{I}z - \mathbf{F}_2)}{z} \mathbf{H}\hat{\mathbf{H}}^{-1}\mathbf{i}_{dq}^*(z) \right] \quad (11)$$

where

$$\begin{aligned} \mathbf{M}_2(z) &= \mathbf{I}z^3 + \left( \hat{\mathbf{G}} - \mathbf{G} - \mathbf{F}_1 - \mathbf{F}_2 \right) z^2 \\ &+ \left\{ \begin{array}{l} \mathbf{H}\hat{\mathbf{H}}^{-1}(\mathbf{I} - \mathbf{F}_1)(\mathbf{I} - \mathbf{F}_2) \\ - (\mathbf{I} + \hat{\mathbf{G}} - \mathbf{G} - \mathbf{F}_1 - \mathbf{F}_2) \\ + (\mathbf{I} + \hat{\mathbf{G}} - \mathbf{F}_1 - \mathbf{F}_2)(\mathbf{H}\hat{\mathbf{H}}^{-1}\hat{\mathbf{G}} - \mathbf{G}) \\ - (\mathbf{I} + \hat{\mathbf{G}} - \mathbf{F}_1 - \mathbf{F}_2)(\mathbf{H}\hat{\mathbf{H}}^{-1}\hat{\mathbf{G}} - \mathbf{G}) \end{array} \right\} z \\ \mathbf{M}_3(z) &= (z-1)\mathbf{H}(\mathbf{I}z + \mathbf{I} + \hat{\mathbf{G}} - \mathbf{F}_1 - \mathbf{F}_2). \end{aligned}$$

As shown in Fig. 2, the application of the incremental model provides a built-in integrator in the forward channel of the control loop. Consequently, the output static currents of RI-DPCC are determined by the static gain of the feedback channel, whose final value is  $\mathbf{I}$  regardless of parameter mismatches. Meanwhile, the factor  $(z-1)$  in  $\mathbf{M}_3(z)$  can cancel the poles of step signals. Therefore, the component

corresponding to voltage errors in DC form, including  $\Psi(z)$  at constant speeds, in the output will decline to zero within a finite time according to the final value theorem. Thus, RI-DPCC is able to eliminate static current errors caused by either parameter mismatches or the DC component of  $e_{dq}(z)$  when the current loop remains stable. Additionally, by substituting matched estimated motor parameters into (11),  $\mathbf{M}_2(z)$  can be simplified to  $z(\mathbf{I}z - \mathbf{F}_1)(\mathbf{I}z - \mathbf{F}_2)$ . Therefore, as a result of the pole-zero cancellation, the ideal performance of RI-DPCC can still be described as  $\mathbf{i}_{dq}(z) = z^{-2}\mathbf{i}_{dq}^*(z)$  after  $\mathbf{M}_2^{-1}(z)\mathbf{M}_3(z)e_{dq}(z)$  declines to zero, ignoring voltage ripples.

For stability analysis, by applying the same approximations as in II.B, (11) can be approximated to (12). It can be seen that although the stable range of  $dq$ -axis currents can be set separately by adjusting feedforward coefficients, the stability of the current loop under RI-DPCC is ultimately determined by the narrower range between them due to the presence of coupling. The selection of feedforward coefficients should follow the principle that the current loop remains stable under matched estimated motor parameters, resulting in an optional range of  $(-1, 1)$ . The stable ranges under different combinations of feedforward coefficients can be obtained based on (12), and several numerical examples are provided in (13), where all the feedforward coefficients are set to a unified value  $f$ .

$$\begin{aligned} \begin{bmatrix} i_d(z) \\ i_q(z) \end{bmatrix} &\approx \underbrace{\begin{bmatrix} A_{2d}(z)B_{2d}(z) \\ A_{2q}(z)B_{2q}(z) \end{bmatrix}}_{coupling\ part} \\ &+ A_{2d}(z)A_{2q}(z)(z-1)T_s\omega_e \begin{bmatrix} -C_{2q}(z)B_{2q}(z) \\ C_{2d}(z)B_{2d}(z) \end{bmatrix} \quad (12) \end{aligned}$$

where

$$A_{2d(2q)}(z) = \left\{ \begin{array}{l} z^3 - (f_{d1(q1)} + f_{d2(q2)})z^2 \\ + (3 - 2f_{d1(q1)} - 2f_{d2(q2)} + f_{d1(q1)}f_{d2(q2)})\delta L_{d(q)}z \\ + f_{d1(q1)}f_{d2(q2)}z - (2 - f_{d1(q1)} - f_{d2(q2)})\delta L_{d(q)} \end{array} \right\}^{-1}$$

$$\begin{aligned} B_{2d(2q)}(z) \\ = \frac{(z - f_{d1(q1)})(z - f_{d2(q2)})}{z} \frac{\hat{L}_{d(q)}\mathbf{i}_{dq}^*(z)}{L_{d(q)}} \\ - \frac{T_s}{L_{d(q)}}(z-1)(z+2-f_{d1(q1)}-f_{d2(q2)})e_{dq}(z) \end{aligned}$$

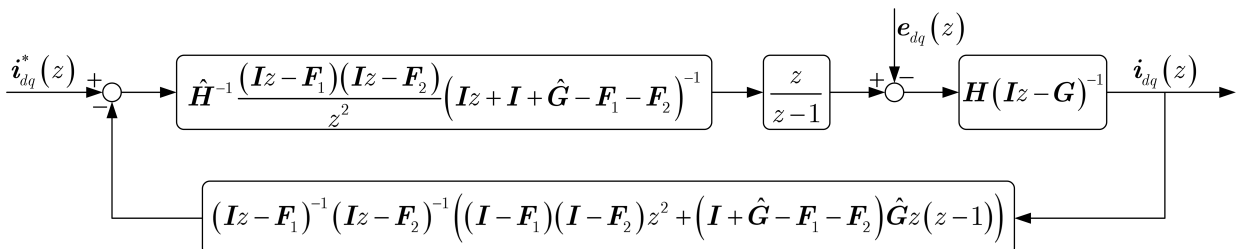


Fig. 2. Control block diagram of the current loop under RI-DPCC.

$$\begin{aligned}
 C_{2d(2q)}(z) &= \left( \frac{\hat{L}_{d(q)}}{\hat{L}_{q(d)}} - \frac{L_{d(q)}}{L_{q(d)}} \right) z \\
 &+ \frac{\hat{L}_{d(q)}}{\hat{L}_{q(d)}} \delta L_{q(d)} + \frac{L_{d(q)}}{L_{q(d)}} (2 - f_{d1(q1)} - f_{d2(q2)}) \delta L_{d(q)}. \\
 &\quad \left\{ \begin{array}{ll} 0.8 < \hat{L}_{d(q)}/L_{d(q)} < 1.25 & (f=0) \\ 0 < \hat{L}_{d(q)}/L_{d(q)} < 2 & (f=0.6) \\ 0 < \hat{L}_{d(q)}/L_{d(q)} < 3 & (f=0.778) \\ 0 < \hat{L}_{d(q)}/L_{d(q)} < 4 & (f=0.846) \\ 0 < \hat{L}_{d(q)}/L_{d(q)} < 5 & (f=0.882) \end{array} \right. \quad (13)
 \end{aligned}$$

When  $f = 0$ , it can be seen that the stable range of I-DPCC is significantly narrower compared to C-DPCC, which limits its practical application. Fig. 3 shows the theoretical stable range of the current loop under RI-DPCC when adopting different combinations of feedforward coefficients, where only those wider than the stable range of I-DPCC are exhibited. Different feedforward coefficient combinations that yield the same stable range are displayed on the plane where  $z = -1$ . It can be seen that larger values of feedforward coefficients result in a larger stable range. When given a constant  $f_{d1(q1)} + f_{d2(q2)}$ , a slightly larger stable range can be obtained by enlarging  $|f_{d1(q1)} - f_{d2(q2)}|$ . Both (12) and the symmetry of Fig. 3 clarify that  $f_{d1(q1)}$  is equivalent to  $f_{d2(q2)}$ , if the voltage limitation is not considered. However, although the combination of feedforward control can effectively extend the stable range of the current loop, the deterioration of dynamic performance under inductance errors is still inevitable.

Additionally, the ability of the current loop to suppress voltage disturbances in AC form under matched estimated motor parameters can be analyzed based on  $G_{d(q)}(z)$ , the transfer function from  $e_{d(q)}(z)$  to  $i_{d(q)}(z)$  in (14), since (12) can be further approximated to (14) if the coupling part is temporarily ignored. The Bode diagram of  $G_{d(q)}(z)$  under unified feedforward coefficients that yield different stable ranges is shown in Fig. 4, where  $T_s$  is set to  $10^{-4}$ s. It can be seen that the ability of the current loop to suppress low-frequency voltage disturbances decreases significantly with the extension of stable range. Therefore, the selection of feedforward coefficients should comprehensively consider the suppression of ripples rather than solely focus on achieving a larger stable range.

$$i_{d(q)}(z) = \frac{1}{z^2} i_{d(q)}^*(z) - \frac{1}{L_{d(q)}} G_{d(q)}(z) e_{d(q)}(z) \quad (14)$$

$$\text{where } G_{d(q)}(z) = T_s \frac{(z-1)(z+2-f_{d1(q1)}-f_{d2(q2)})}{z(z-f_{d1(q1)})(z-f_{d2(q2)})}.$$

### C. Dynamic Performance Improvement by Inductance Correction

The relatively larger stable range provided by RI-DPCC makes it possible to further improve the dynamic performance under inductance errors using the method proposed in this section. Next, the proposed inductance correction method will be explained based on its application example in a dynamic process with a step in the  $q$ -axis current command.

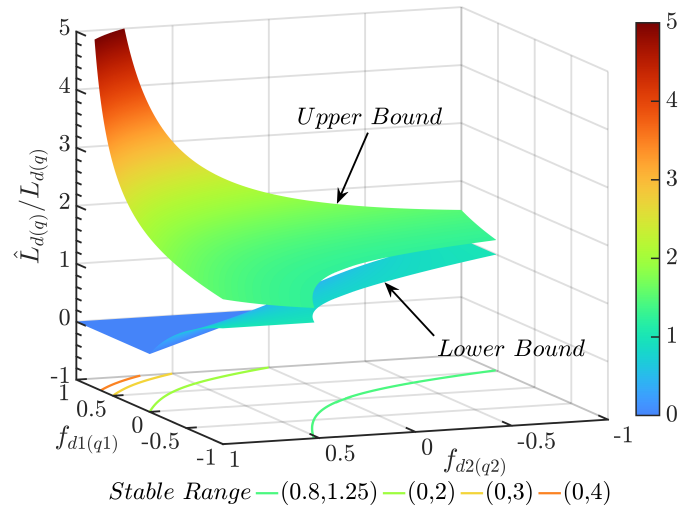


Fig. 3. Theoretical stable range of the current loop under RI-DPCC when adopting different combinations of feedforward coefficients.

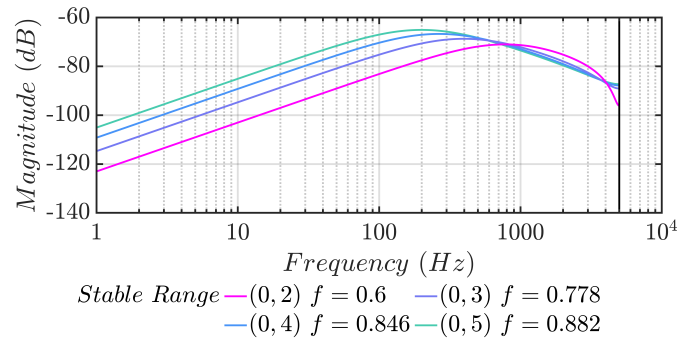


Fig. 4. Bode diagram of  $G_{d(q)}(z)$  under unified feedforward coefficients that yield different stable ranges.

The schematic diagram of the correction process is shown in Fig. 5. Suppose the current loop has already reached a steady state without static current errors under mismatched  $\hat{L}_q$  within its stable range before  $i_q^*$  steps from  $i_q^*(k-3)$  to  $i_q^*(k-2)$  at the  $(k-2)^{th}$  instant, and  $i_q^*$  will remain constant at  $i_q^*(k-2)$  after the step.

During the  $(k-2)^{th}$  control period,  $i_q$  remains constant as a result of the unit computation delay. Then, it undergoes variation during the  $(k-1)^{th}$  control period under the effect of  $u_q^*(k-1)$ , which is calculated to drive  $i_q$  to reach  $i_q^*(k-2)$  at the  $k^{th}$  instant. However, the value of  $i_q(k)$  it reaches will deviate from  $i_q^*(k-2)$  due to the presence of inductance error. After that, during the  $k^{th}$  control period, as the regulator wrongly assumes that  $i_q$  will reach  $i_q^*(k-2)$  at the  $k^{th}$  instant, the  $u_q^*(k)$  it calculates will maintain  $i_q$  almost constant during the  $k^{th}$  control period.

If the mismatched  $\hat{L}_q$  can be corrected to  $L_q$  based on the response of currents during the  $(k-1)^{th}$  control period and adopted in the calculation of  $u_q^*(k+1)$ ,  $i_q$  will be able to reach  $i_q^*(k-2)$  at the  $(k+2)^{th}$  instant. Thus, with sufficient voltage margin, the tracking delay under mismatched inductance can be shortened to its theoretical minimum of  $4T_s$ , although overshoot is unavoidable for an  $\hat{L}_q$  larger than  $L_q$ .

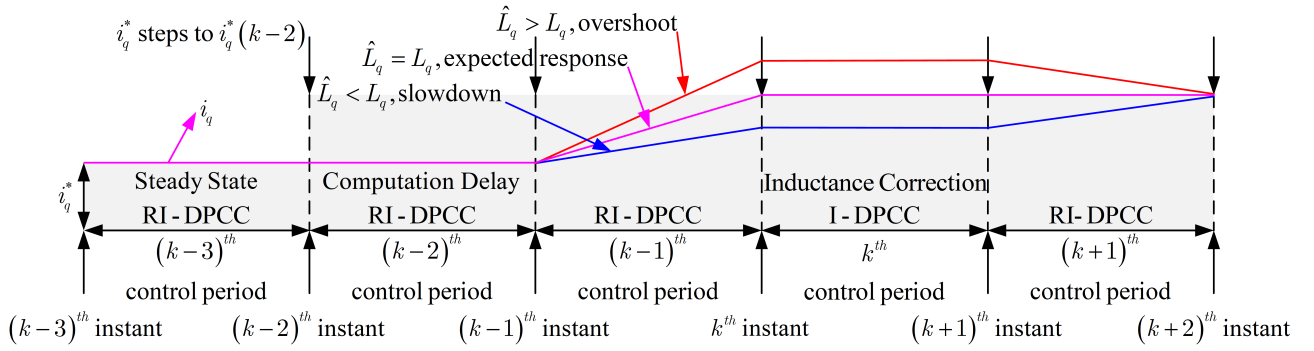


Fig. 5. Schematic diagram of the inductance correction when applied in a dynamic process with a step in the  $q$ -axis current command.

By rearranging the expression of  $\Delta i_{dq}(k)$  in (8),  $L_d$  and  $L_q$  can be expressed as (15). Since all the values on the right side of the equation are available during the  $k^{th}$  control period, the corresponding actual inductance can theoretically be obtained based solely on the significant variation of currents during the previous control period. Consequently, the desired tracking delay of  $4T_s$  mentioned above can be achieved by fully accepting the corrected result to update the estimated inductance.

$$\begin{bmatrix} L_d \\ L_q \end{bmatrix} = \frac{T_s}{A_{4d}A_{4q} + A_{5d}A_{5q}} \begin{bmatrix} A_{3d}A_{4q} + A_{3q}A_{5q} \\ A_{3q}A_{4d} - A_{3d}A_{5d} \end{bmatrix} \quad (15)$$

where

$$A_{3d(q)} = \Delta u_{d(q)}(k-1) - R\Delta i_{d(q)}(k-1)$$

$$A_{4d(q)} = \Delta i_{d(q)}(k) - \Delta i_{d(q)}(k-1)$$

$$A_{5d(q)} = T_s\omega_e(k-1)\Delta i_{d(q)}(k-1).$$

In practical applications, inductance correction can be conducted during the  $k^{th}$  control period after substituting  $\Delta u_{d(q)}^*(k-1)$  and  $R$  into (15). However, it should be noted that when incremental values approach 0 in steady state, the information of actual inductances contained in them will be submerged in ripples and become difficult to extract. To avoid mis-correction, it is necessary to set a threshold to distinguish dynamic processes with significant

current variations from ripples. The correction for the  $d(q)$ -axis inductance can be set to trigger when  $|\Delta u_{d(q)}^*(k-1)|$  or  $|\Delta i_{d(q)}(k) - \Delta i_{d(q)}(k-1)|$  is detected to be larger than the threshold, as their amplitudes are positively correlated. Alternatively, using  $|i_{d(q)}^*(k-2) - i_{d(q)}^*(k-3)|$  is also feasible due to the characteristic of DPCC.

Furthermore, during the control period when inductance correction is triggered, the feedforward coefficients should be set to 0, i.e., the control method is switched from RI-DPCC to I-DPCC. Otherwise, the prediction errors from the previous control period will continue to have an impact as the result of inopportune feedforward. Due to disturbance factors like voltage and current ripples, the corrected results will fluctuate around the actual inductances, which is acceptable under RI-DPCC but may cause instability under I-DPCC. Therefore, for stability, the control method should be switched back to RI-DPCC from the next control period after inductance correction has been triggered.

An overall control block diagram of the proposed RI-DPCC with inductance correction is shown in Fig. 6. During each control period, the system first detects whether the variation of currents from the previous control period meets the trigger condition for inductance correction, thus correcting  $\hat{L}_{d,q}$  using (15) or keeping them unchanged. Subsequently, feedforward coefficients will be adjusted based on whether inductance cor-

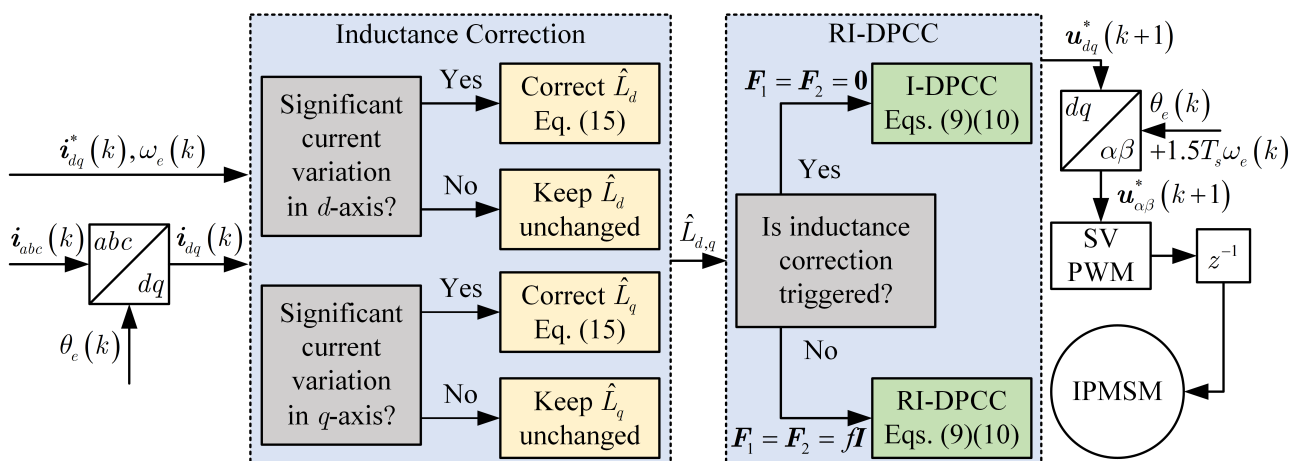


Fig. 6. Overall control block diagram of the proposed RI-DPCC with inductance correction.

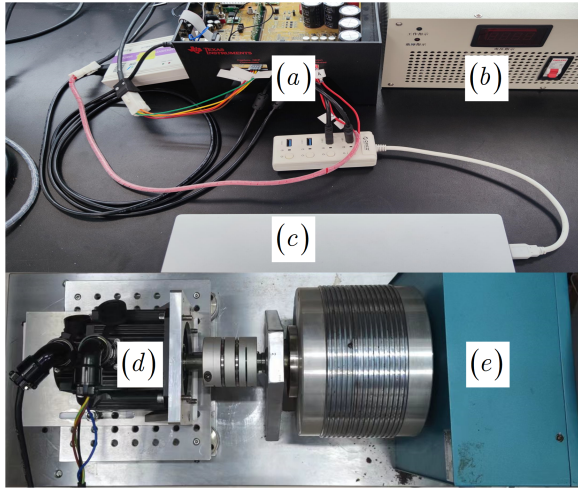


Fig. 7. Experimental platform. (a) TMDSHVMTRPFC kit. (b) Power supply. (c) PC. (d) Test IPMSM. (e) Dynamometer.

TABLE I  
PARAMETERS OF THE TEST IPMSM AND EXPERIMENTS

Parameter	Symbol	Value
Nominal stator resistance	$R_0$	1.7 Ω
Nominal $d$ -axis inductance	$L_{d0}$	10.5 mH
Nominal $q$ -axis inductance	$L_{q0}$	14.8 mH
Saturated $q$ -axis inductance under $i_s = 12A$		$0.57L_{q0}$
Nominal rotor flux linkage	$\psi_{f0}$	0.196 Wb
Pole pairs	$p$	4
DC bus voltage	$V_{DC}$	350 V
Control period of the current/speed loop	$T_s/5T_s$	0.1/0.5 ms
Dead time		2 μs

rection is triggered, and voltage commands are then calculated accordingly using (9) and (10).

#### IV. EXPERIMENTAL RESULTS

To validate the effectiveness of the proposed method, experiments were performed on the platform shown in Fig. 7, which was constructed based on TI's TMDSHVMTRPFC kit with the TMS320F28335 processor. The experiments were

conducted in the current loop at a constant speed and in the speed loop under a constant load, respectively. The parameters of the test IPMSM and experiments are presented in Table I. Since the  $dq$ -axis inductances of the test IPMSM vary significantly with the  $dq$ -axis currents, their measurement results with a current step of 0.5A are shown in Fig. 8. It should be noted that the nominal values  $L_{d0}$  and  $L_{q0}$  presented in Table I are the measured  $dq$ -axis inductances when  $i_d \in [-2.5A, -2A]$  and  $i_q \in [2A, 2.5A]$ .  $L_{d0}$ ,  $L_{q0}$  and  $\psi_{f0}$  were adopted in the calculation of  $dq$ -axis current commands based on the maximum torque per ampere (MTPA) strategy and  $i_s^*$ , the output stator current command of the speed regulator when conducting experiments in the speed loop. With the increase in stator current  $i_s$ , the measured  $L_q$  gradually decreases and saturates to  $0.57L_{q0}$  under an  $i_s$  of 12A. Additionally, all the feedforward coefficients of RI-DPCC were set to a unified value  $f$  in the experiments for convenience. Furthermore, the phase delay resulting from coordinate transformation was compensated using the method proposed in [23], while the compensation for inverter nonlinearities was based on the method proposed in [24].

#### A. Static Performance and Stability of the Current Loop with Speed Control

Experiments were first conducted in the speed loop of the test motor at a constant speed of 600rpm to validate the effectiveness of the proposed RI-DPCC in static current error elimination and stable range extension. The speed loop adopted a PI regulator, and its control frequency was 1/5 of the current loop. The stator current command  $i_s^*$  was adjusted to a unified value of 4A by modifying the load torque, and the presence of any static error between  $i_s^*$  and  $i_s$  was recorded by the oscilloscope. Subsequently, comparisons of the static performance and stability of the current loop under I-DPCC and RI-DPCC, at different parameter errors and feedforward coefficients, are conducted based on the experimental results shown in Fig. 9.

Fig. 9(a) and (d) illustrate the static waveform of currents under I-DPCC and RI-DPCC with matched estimated motor

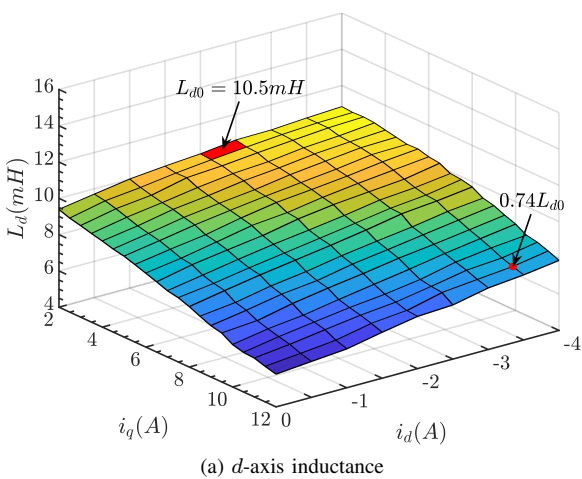
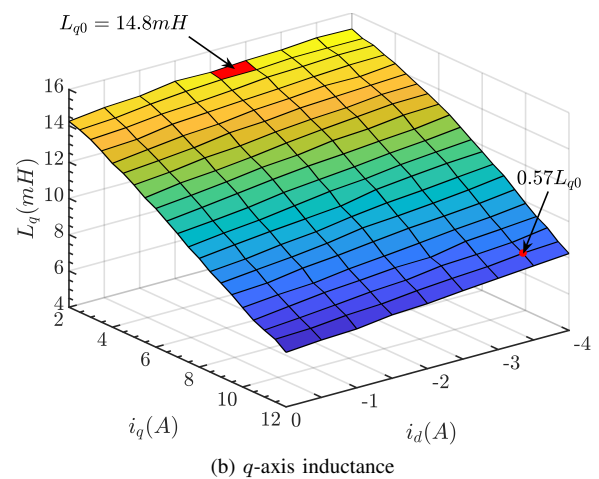


Fig. 8. Measured  $dq$ -axis inductances of the test IPMSM.



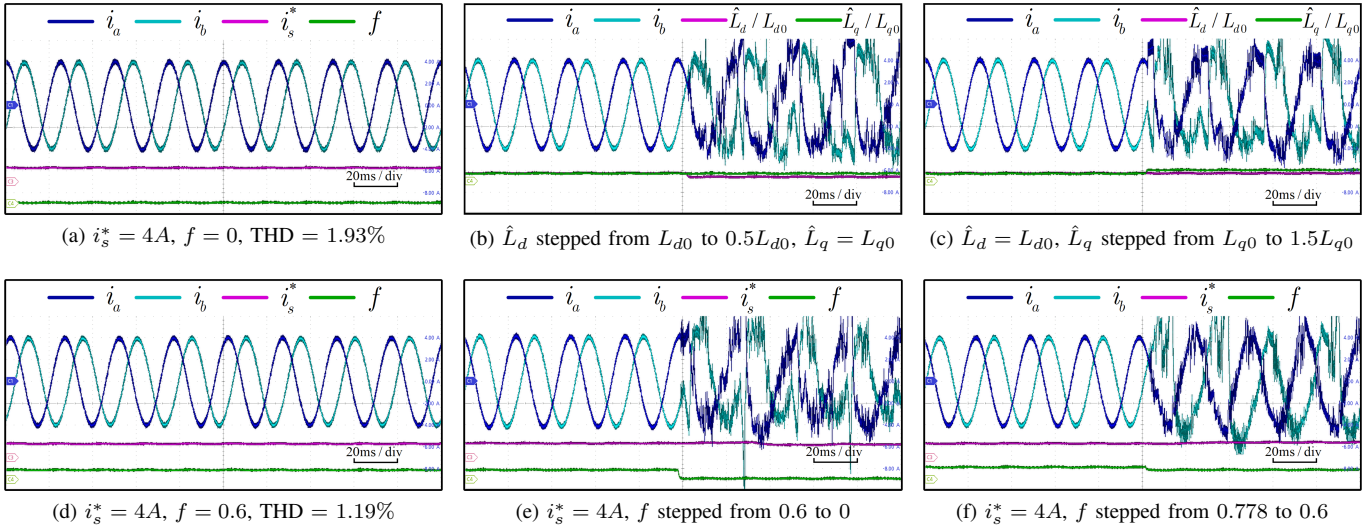


Fig. 9. Experimental results of the static performance and stability of the current loop under I-DPCC and RI-DPCC at different parameter errors and feedforward coefficients. (a)-(c) I-DPCC. (d)-(f) RI-DPCC. (b) Step change of  $\hat{L}_d$ . (c) Step change of  $\hat{L}_q$ . (e)(f) Step change of  $f$ . (a)(d)  $\hat{R} = R_0$ ,  $\hat{L}_d = L_{d0}$ ,  $\hat{L}_q = L_{q0}$ . (b)(c)  $\hat{R} = R_0$ . (e)  $\hat{R} = 0$ ,  $\hat{L}_d = 0.5L_{d0}$ ,  $\hat{L}_q = 1.5L_{q0}$ . (f)  $\hat{R} = 2R_0$ ,  $\hat{L}_d = 2.5L_{d0}$ ,  $\hat{L}_q = 2.5L_{q0}$ .

parameters, respectively. They indicate that both the current loops under I-DPCC and RI-DPCC could achieve zero static current error and low current ripples without requiring knowledge of flux linkage. Additionally, stator currents under the proposed RI-DPCC exhibited lower total harmonic distortion (THD) compared to those under I-DPCC in the test condition.

Fig. 9(b) and (c) illustrate the waveform of currents under I-DPCC before and after a step change of the estimated inductances. When  $\hat{L}_d$  stepped from  $L_{d0}$  to  $0.5L_{d0}$  or  $\hat{L}_q$  stepped from  $L_{q0}$  to  $1.5L_{q0}$ , the current loop became unstable, illustrating the poor stability robustness of I-DPCC.

Fig. 9(e) and (f) illustrate the waveform of currents under RI-DPCC with mismatched estimated resistance and inductances before and after a step change of the stable range achieved by adjusting  $f$ . With the combination of feedforward control, the current loop under RI-DPCC with  $f = 0.6$  remained stable under mismatched inductances  $\hat{L}_d = 0.5L_{d0}$  and  $\hat{L}_q = 1.5L_{q0}$ , which were intolerable for the current loop under I-DPCC. Furthermore, the current loop under RI-DPCC with  $f = 0.778$  was able to remain stable under mismatched inductances  $\hat{L}_d = 2.5L_{d0}$  and  $\hat{L}_q = 2.5L_{q0}$ , a scenario in which even adopting C-DPCC could not stabilize. Notably, zero static current error at mismatched estimated motor parameters was still achieved under RI-DPCC.

#### B. Dynamic Performance of the Current Loop without Speed Control

Experiments were then conducted in the current loop of the test motor with sufficient voltage margin at different constant speeds to validate the effectiveness of the proposed RI-DPCC with inductance correction in improving the robustness of the dynamic performance. Different constant speeds were achieved by using another coaxially connected load motor. The  $dq$ -axis current commands were set with the same amplitude but opposite polarity, and their amplitudes were artificially stepped up from 2A to 2.5A and stepped down

from 2.5A to 2A individually during the experiments. For RI-DPCC,  $f$  was set to 0.6 to achieve the same stable range of the current loop as under C-DPCC. Regarding inductance correction, the threshold for correction triggering was set as  $|i_{d(q)}^*(k-2) - i_{d(q)}^*(k-3)| > 0.3A$ . Subsequently, comparisons of the dynamic performance of the current loop under RI-DPCC with sufficient voltage margin, at different speeds and parameter errors, are conducted based on the experimental results shown in Fig. 10.

Fig. 10(a)-(c) illustrate the dynamic response of currents under single RI-DPCC with matched estimated resistance and different inductance errors at a constant speed of 600rpm. It can be seen that single RI-DPCC achieved zero static current error under inductance errors and a tracking delay of  $2T_s$  under matched estimated motor parameters. However, the dynamic response exhibited overshoots and oscillations under larger  $\hat{L}_{d(q)}$ , while slowing down and overshooting under smaller  $\hat{L}_{d(q)}$ . Therefore, further improvements are required to enhance the robustness of the dynamic performance under RI-DPCC.

Fig. 10(d)-(f) illustrate the dynamic response of currents under RI-DPCC with inductance correction. They were obtained under the same initially adopted estimated motor parameters as the experimental results shown in Fig. 10(a)-(c), respectively, and also at a constant speed of 600rpm. Since the step of current commands occurred at the  $3T_s$  instant, the inductance correction was only triggered and executed during the fifth control period. The values of estimated inductances before and after correction are attached to the labels of the figures. Although the influence of voltage and current ripples caused the corrected results to fluctuate around the actual value, a significant reduction of large inductance errors was achieved. As a result, a tracking delay of  $2T_s$  was almost maintained when matched  $\hat{L}_{d(q)}$  underwent correction in Fig. 10(e). And the tracking delay under larger or smaller  $\hat{L}_{d(q)}$  could both be shortened to  $4T_s$  as shown in Fig. 10(d) and (f), which was

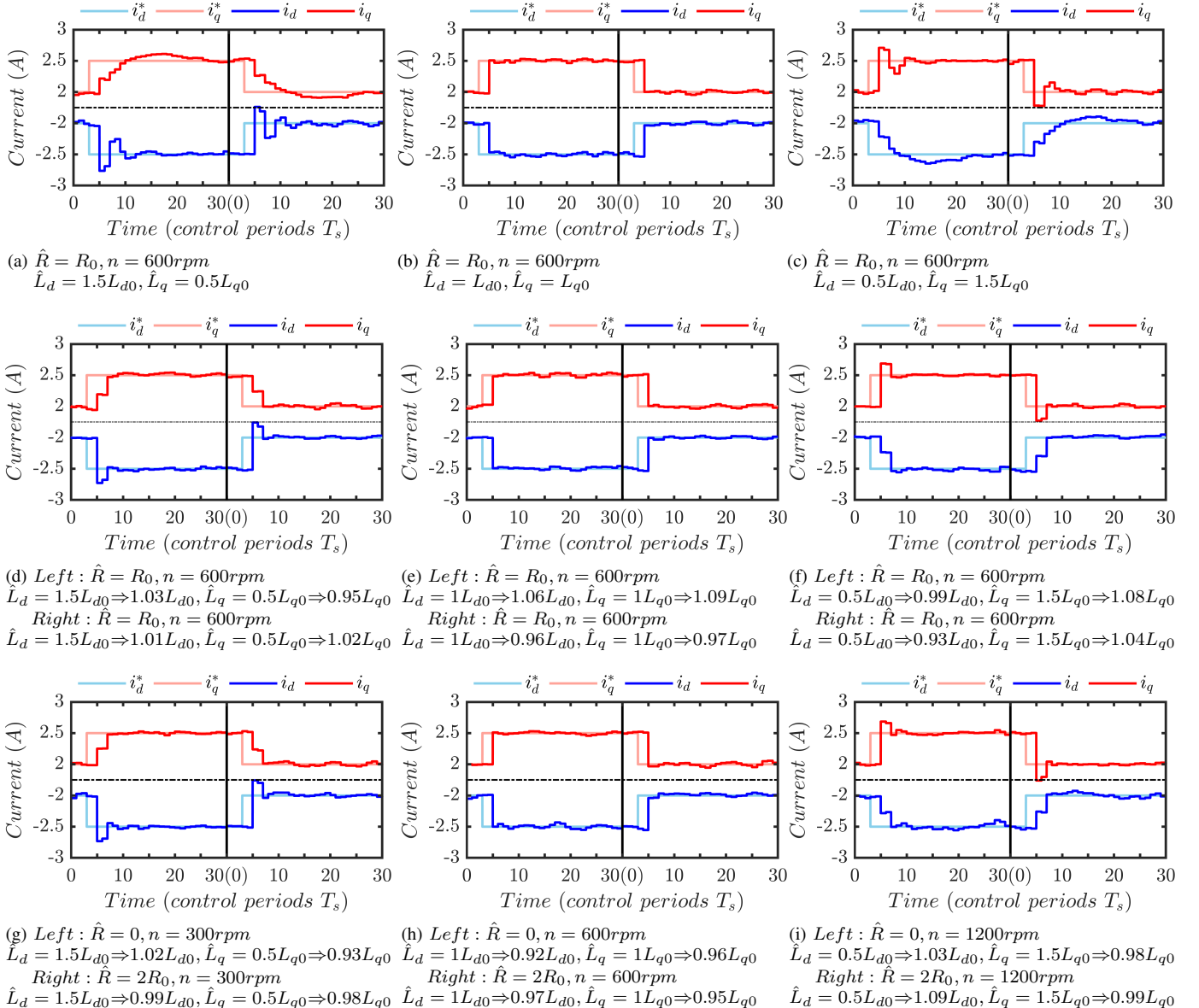


Fig. 10. Experimental results of the dynamic performance of the current loop under RI-DPCC with sufficient voltage margin at different speeds and parameter errors. (a)-(c) Single RI-DPCC. (d)-(i) RI-DPCC with inductance correction.

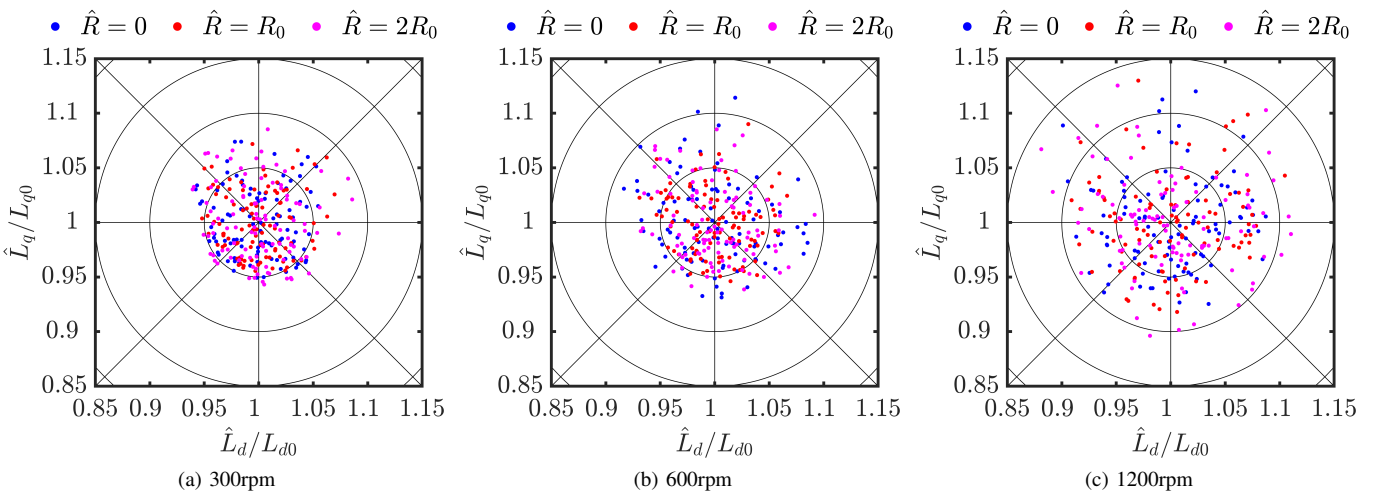


Fig. 11. Experimental results of 100 parallel inductance corrections at different speeds and resistance errors.

significantly improved compared to single RI-DPCC.

Considering the potential resistance errors and different speeds in practical applications, experimental results shown in Fig. 10(g)-(i) were obtained individually at constant speeds of 300rpm, 600rpm and 1200rpm while introducing resistance errors within a reasonable range. Their initially adopted estimated inductances were still the same as the experimental results shown in Fig. 10(a)-(c), respectively. Comparing Fig. 10(e) and (h), it can be seen that a tracking delay of  $2T_s$  was still almost maintained even when mismatched estimated resistances were adopted. Additionally, the experimental results shown in Fig. 10(g) and (i) further validate the effectiveness of the proposed method, as a tracking delay of  $4T_s$  was still achieved at different speeds under mismatched estimated resistance and inductances.

Since the value of  $\hat{R}\Delta i_{d(q)}(k-1)$  is much smaller than  $\Delta u_{d(q)}^*(k-1)$  when inductance correction is triggered, resistance errors within a reasonable range have little impact on the corrected results and dynamic performance. To further demonstrate this conclusion, Fig. 11 illustrates the results of 100 parallel corrections at different speeds and resistance errors, conducted under the same current commands as in Fig. 10. The values of  $\hat{R}$  were set as 0,  $R_0$ , and  $2R_0$  individually. It can be seen from Fig. 11 that resistance errors within a reasonable range have little impact on the distribution of correction results. The relative error of most correction results is within  $\pm 10\%$  at 300rpm and 600rpm. However, it increases to  $\pm 15\%$  at 1200rpm due to the ripples of voltage and current, which increase with the speed. While the impact of small inductance errors on dynamic performance remains within an acceptable range as shown in Fig. 10(i), the suppression of ripples becomes more crucial with the increase in speed.

### C. Dynamic Performance of the Current Loop with Speed Control during a Speed-Up Process

Experiments were further conducted in the speed loop of the test motor to validate the effectiveness of the proposed method in a dynamic process with significant inductance variation. The test motor initially operated at 600rpm with a constant load corresponding to an  $i_s$  of 4A before the speed command stepped from 600rpm to 900rpm. The control frequency of the speed loop was still 1/5 of the current loop, and the stator current limit was set to 12A. All the initially adopted estimated motor parameters were set to their nominal values presented in Table I. Subsequently, comparisons of the dynamic performance of the current loop under four different current control methods during a speed-up process are conducted based on the experimental results shown in Fig. 12.

Fig. 12(a) illustrates the dynamic response of currents under C-DPCC during the speed-up process. When a significant step increase occurred in  $i_s^*$ , the corresponding dynamic process lasted more than  $2T_s$  due to the voltage limitation. As a result of saturation and coupling, the unchanged  $\hat{L}_q = L_{q0}$  became significantly larger than the actual  $L_q$ , leading to the appearance of overshoots and oscillations in  $dq$ -axis currents. Additionally, overshoots also appeared when the currents dropped from the limit due to the same reason.

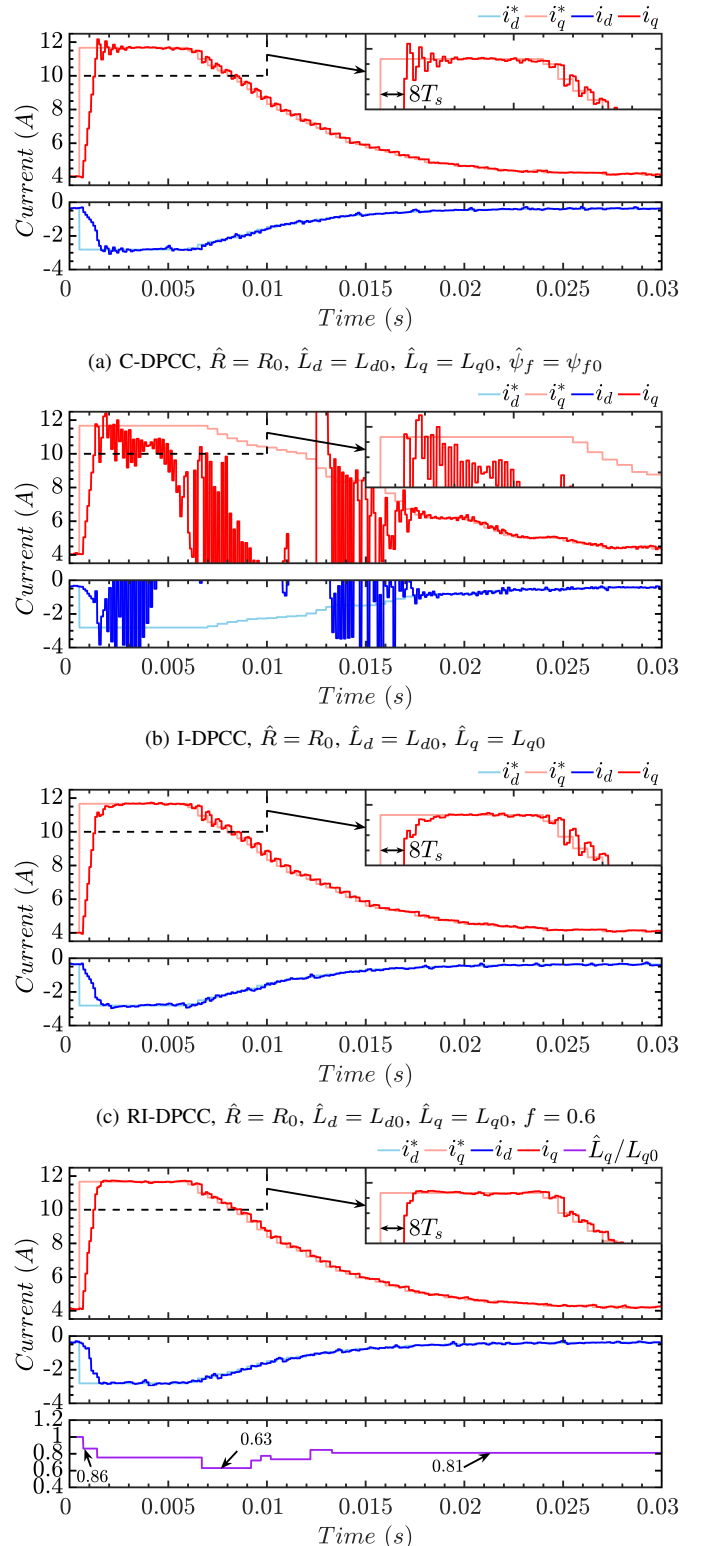


Fig. 12. Experimental results of the dynamic performance of the current loop under different current control methods during a speed-up process.

Fig. 12(b) illustrates the dynamic response of currents under I-DPCC during the speed-up process. As the actual inductance saturated to a level below its narrow stable range, the current

loop lost control under heavy load, which is considered unacceptable for high-performance control.

Fig. 12(c) illustrates the dynamic response of currents under single RI-DPCC during the speed-up process. Since the current commands could not be tracked with a delay of  $2T_s$  due to the voltage limitation, the introduction of feedforward values in the voltage command calculation equations caused the regulator to exit saturation prematurely. And its impact continued to take effect until the currents reached their commands under the action of the built-in integrator, resulting in a slowdown of the dynamic response. Although modifying current commands can compensate for this issue in motors with relatively fixed inductances, it proves to be less effective in cases where the inductance varies significantly. Therefore, the response shown in Fig. 12(c) was a combination of the aforementioned issue and inductance saturation, and overshoots were still inevitable when currents dropped from the limit.

Fig. 12(d) illustrates the dynamic response of currents under RI-DPCC with inductance correction during the speed-up process. Since the variation of  $L_d$  did not have a significant impact on the  $d$ -axis current under RI-DPCC, only the variation of  $L_q$  was focused on. The threshold for correction triggering was set as  $|\Delta u_q^*(k-1)| > 30V$  instead of  $|i_q^*(k-2) - i_q^*(k-3)| > 0.3A$ , so the inductance correction could be triggered multiple times during the dynamic process of a significant step in current command to better track the variation of  $L_q$ . Since inductance correction was triggered again when the regulator exited saturation, the control method was temporarily switched to I-DPCC with corrected  $\hat{L}_q$ . As a result,  $i_q$  was able to reach the command in a shorter time without oscillations and overshoots compared to Fig. 12(c). Additionally, under the effect of inductance correction,  $i_q$  essentially tracked the command with a delay of  $2T_s$  during the dropping process. Although the final value of  $\hat{L}_q$  did not converge to the actual  $L_q$  due to the presence of the threshold, zero static current error was still achieved by the application of RI-DPCC. And minor inductance errors will be corrected at the beginning of the next significant dynamic process, whose overall impact is considered acceptable. In conclusion, the proposed method can effectively improve the dynamic performance of IPMSMs with significant inductance variation.

## V. CONCLUSION

A robust incremental model-based DPCC method with inductance correction is proposed in this paper to improve the robustness of the current loop for IPMSMs. And experimental results validate its effectiveness.

The major merits of this method include:

- 1) The application of the incremental motor model eliminates the use of rotor flux linkage in the control equations and provides a built-in integrator in the current loop. Therefore, zero static current error can be achieved even under mismatched parameters.
- 2) The stable range of the current loop can be effectively extended by combining feedback control with feedforward control. Four adjustable feedforward coefficients are introduced, and the impact of their values is theoretically analyzed. Thus, the stable range can be dynamically adjusted as needed.

3) By adopting inductance correction, the variation of inductance during dynamic processes can be tracked in real-time. Thus, the current commands can be well tracked even when significant inductance variation occurs. With sufficient voltage margin, the dynamic processes under mismatched inductance can be shortened to four control periods while maintaining a tracking delay of two control periods under accurate motor parameters.

## REFERENCES

- [1] P. Wipasuramonton, Z. Q. Zhu and D. Howe, "Predictive current control with current-error correction for PM brushless AC drives," *IEEE Trans. Ind. Appl.*, vol. 42, no. 4, pp. 1071-1079, Jul.-Aug. 2006.
- [2] P. Cortes, J. Rodriguez, C. Silva and A. Flores, "Delay compensation in model predictive current control of a three-phase inverter," *IEEE Trans Ind. Electron.*, vol. 59, no. 2, pp. 1323-1325, Feb. 2012.
- [3] Weihua Wang and Xiao Xi, "Current control method for PMSM with high dynamic performance," *2013 Int. Electr. Mach. & Drives Conf.*, 2013, pp. 1249-1254.
- [4] L. He, F. Wang, J. Wang and J. Rodríguez, "Zynq implemented Luemburger disturbance observer based predictive control scheme for PMSM drives," *IEEE Trans. Power Electron.*, vol. 35, no. 2, pp. 1770-1778, Feb. 2020.
- [5] L. Rovere, A. Formentini and P. Zanchetta, "FPGA implementation of a novel oversampling deadbeat controller for PMSM drives," *IEEE Trans Ind. Electron.*, vol. 66, no. 5, pp. 3731-3741, May 2019.
- [6] G. Pei, J. Liu, X. Gao, W. Tian, L. Li and R. Kennel, "Deadbeat predictive current control for SPMSM at low switching frequency with moving horizon estimator," *IEEE J. Emerging Sel. Top. Power Electron.*, vol. 9, no. 1, pp. 345-353, Feb. 2021.
- [7] Hoang Le-Huy, K. Slimani and P. Viarouge, "Analysis and implementation of a real-time predictive current controller for permanent-magnet synchronous servo drives," *IEEE Trans. Ind. Electron.*, vol. 41, no. 1, pp. 110-117, Feb. 1994.
- [8] Z. Wang, A. Yu, X. Li, G. Zhang and C. Xia, "A novel current predictive control based on fuzzy algorithm for PMSM," *IEEE J. Emerging Sel. Top. Power Electron.*, vol. 7, no. 2, pp. 990-1001, Jun. 2019.
- [9] X. Zhang and X. Huang, "An incremental deadbeat predictive current control method for PMSM with low sensitivity to parameter variation," *2020 Int. Conf. Electr. Mach.*, 2020, pp. 1060-1066.
- [10] X. Zhang, L. Zhang and Y. Zhang, "Model predictive current control for PMSM drives with parameter robustness improvement," *IEEE Trans. Power Electron.*, vol. 34, no. 2, pp. 1645-1657, Feb. 2019.
- [11] H. Xu, X. Gui, T. Luan, X. Lang and D. Xu, "A robust predictive current controller with incremental model and inductance observer for PMSM drive," *2017 IEEE Transp. Electrif. Conf. Expo, Asia-Pacific*, 2017, pp. 1-6.
- [12] C. Xu, Z. Han and S. Lu, "Deadbeat predictive current control for permanent magnet synchronous machines with closed-form error compensation," *IEEE Trans. Power Electron.*, vol. 35, no. 5, pp. 5018-5030, May 2020.
- [13] X. Zhang, B. Hou and Y. Mei, "Deadbeat predictive current control of permanent-magnet synchronous motors with stator current and disturbance observer," *IEEE Trans. Power Electron.*, vol. 32, no. 5, pp. 3818-3834, May 2017.
- [14] Y. Xu, S. Li and J. Zou, "Integral sliding mode control based deadbeat predictive current control for PMSM drives with disturbance rejection," *IEEE Trans. Power Electron.*, vol. 37, no. 3, pp. 2845-2856, Mar. 2022.
- [15] L. Wang, J. Zhao, X. Yang, Z. Zheng, X. Zhang and L. Wang, "Robust deadbeat predictive current regulation for permanent magnet synchronous linear motor drivers with parallel parameter disturbance and load observer," *IEEE Trans. Power Electron.*, vol. 37, no. 7, pp. 7834-7845, Jul. 2022.
- [16] M. Yang, X. Lang, J. Long and D. Xu, "Flux immunity robust predictive current control with incremental model and extended state observer for PMSM drive," *IEEE Trans. Power Electron.*, vol. 32, no. 12, pp. 9267-9279, Dec. 2017.
- [17] X. Li, S. Zhang, Y. Zhou and C. Zhang, "An improved deadbeat predictive current control scheme for open-winding permanent magnet synchronous motors drives with disturbance observer," *IEEE Trans. Power Electron.*, vol. 36, no. 4, pp. 4622-4632, Apr. 2021.

- [18] P. Kakosimos and H. Abu-Rub, "Deadbeat predictive control for PMSM drives with 3-L NPC inverter accounting for saturation effects," *IEEE J. Emerging Sel. Top. Power Electron.*, vol. 6, no. 4, pp. 1671-1680, Dec. 2018.
- [19] Y. Yu et al., "Full parameter estimation for permanent magnet synchronous motors," *IEEE Trans. Ind. Electron.*, vol. 69, no. 5, pp. 4376-4386, May 2022.
- [20] Y. Zhou, S. Zhang, C. Zhang, X. Li, X. Li and X. Yuan, "Current prediction error based parameter identification method for SPMSM with deadbeat predictive current control," *IEEE Trans. Energy Convers.*, vol. 36, no. 3, pp. 1700-1710, Sept. 2021.
- [21] E. I. Jury, "A note on the modified stability table for linear discrete time systems," *IEEE Trans. Circuits Syst.*, vol. 38, no. 2, pp. 221-223, Feb. 1991.
- [22] J. Stumper, V. Hagenmeyer, S. Kuehl and R. Kennel, "Deadbeat control for electrical drives: a robust and performant design based on differential flatness," *IEEE Trans. Power Electron.*, vol. 30, no. 8, pp. 4585-4596, Aug. 2015.
- [23] Bon-Ho Bae and S. -K. Sul, "A compensation method for time delay of full-digital synchronous frame current regulator of PWM AC drives," *IEEE Trans. Ind. Appl.*, vol. 39, no. 3, pp. 802-810, May-Jun. 2003.
- [24] Jong-Woo Choi and S. -K. Sul, "Inverter output voltage synthesis using novel dead time compensation," *IEEE Trans. Power Electron.*, vol. 11, no. 2, pp. 221-227, Mar. 1996.